Sheath model for radio-frequency-biased, high-density plasmas valid for all ω/ω_i

Mark A. Sobolewski
National Institute of Standards and Technology, Gaithersburg, Maryland 20899-8362
(Received 11 July 2000)

A model is proposed for sheaths in high-density discharges, with radio-frequency (rf) bias applied at frequencies ω comparable to ω_i, the ion plasma frequency at the edge of the sheath. The model treats ion dynamics using fluid equations, including all time-dependent terms. Model predictions for current, impedance, and power were compared to measurements performed in high-density discharges in argon at 1.33 Pa (10 mTorr) at rf bias frequencies from 0.1 to 10 MHz (ω/ω_i from 0.006 to 1.8) and rf bias voltages from 1 to 200 V. Model predictions were in good agreement with measurements, much better than that obtained by models that neglect time-dependent ion dynamics. In particular, differences of as much as 40–50 % between power measurements and the power predicted by previous models are now explained and eliminated. The model also explains why methods of extracting plasma parameters from electrical measurements using previous sheath models may fail, and it suggests more accurate methods of extracting these parameters.

PACS number(s): 52.65.−y

I. INTRODUCTION

The electrical properties of radio-frequency discharges have been the subject of much investigation [1–32]. A major goal of these efforts has been to obtain models that relate electrical characteristics to physical properties such as ion energies [1,2], ion flux [3–6], electron temperature [7], or electron density [7,8], thus enabling electrical measurements to monitor these properties. Models of the space-charge sheath regions adjacent to electrode surfaces are particularly important, since the sheaths usually make dominant contributions to discharge electrical characteristics.

Many sheath models have been proposed [9–30], but their predictions are often contradictory and rarely tested by experiment. ''High-frequency'' sheath models [9–19] cover the regime where the applied rf frequency ω is much greater than ω_i, the ion plasma frequency at the edge of the sheath. For $\omega \gg \omega_i$, the ions, due to their inertia, are unable to respond to the rf electric field; rather, they only follow the time-averaged field. High-frequency models agree with sheath impedance measurements performed in capacitively coupled, low-density plasma reactors [15,31]. In contrast, in high-density plasmas, $\omega < \omega_i$ or $\omega \approx \omega_i$, and thus the ions do respond to the rf electric field. Models [23–27] proposed for the regime $\omega \leqslant \omega_i$, however, treat the time-dependent ion motion using assumptions that are valid only for $\omega \ll \omega_i$. The failure of such models to fully account for time-dependent ion dynamics casts doubt on their predictions and may explain why they disagree with experimental measurements of rf current [32] and power [25].

This article presents a sheath model that does fully account for time-dependent ion motion. The model is designed to simulate sheaths in high-density, low-pressure discharges, in particular, the sheath at the rf-biased, lower electrode of the inductively coupled gaseous electronics conference (GEC) reference cell [33] for high-density discharges in argon at pressures ≈1.33 Pa (10 mTorr). These discharges have been particularly well characterized by many measurement techniques [6,25,32–39]. Using these previous experimental results, we rigorously test the model, and show that it agrees with experiment better and over a wider range than previous models.

First, in Sec. II, the model is described, including its assumptions, its method of solution, and the experimental values of its input parameters. Then, in Sec. III, model predictions for the current, impedance, and power are presented and compared with previous models and with experiment. Section IV discusses several useful extensions of the model and Sec. V summarizes the results.

II. SHEATH MODEL

The sheath model is one dimensional. Position is indicated by a single coordinate x. As shown in Fig. 1, the x axis extends from an arbitrary position ($x = x_n$) on the plasma side of the sheath to the surface of the rf-biased electrode ($x = x_{pe}$). Gradients in directions other than x, i.e., parallel to the electrode surface, are ignored.

For high-density argon discharges in the inductive GEC cell, we may neglect all negative ions and all positive ions except Ar^+, which constitutes 98% of the positive ion flux [39]. Thus the sheath contains electrons, with mass m_e and charge $-e$, and a single species of ion, with mass $m_i = 40$ amu and charge $+e$. The electron density $n_e(x,t)$ and the ion density $n_i(x,t)$ both vary with time t as well as position x. They are related to the electric field $E(x,t)$ and the electrostatic potential $V(x,t)$ by Poisson's equation and Gauss's law, i.e.,

$$-\partial V^2/\partial x^2 = \partial E/\partial x = e(n_i - n_e)/\varepsilon_0, \tag{1}$$

where ε_0 is the permittivity of vacuum. The voltage reference is chosen so that $V = 0$ at the center of the plasma. For all x, $n_i \geqslant n_e$, $E \geqslant 0$, and $V \leqslant 0$.

Ion dynamics are modeled using the fluid equations for ion momentum conservation,

$$\partial u_i/\partial t + u_i \partial u_i/\partial x = eE/m_i, \tag{2}$$

and ion conservation,

$$\partial(n_i u_i)/\partial x = -\partial n_i/\partial t, \tag{3}$$

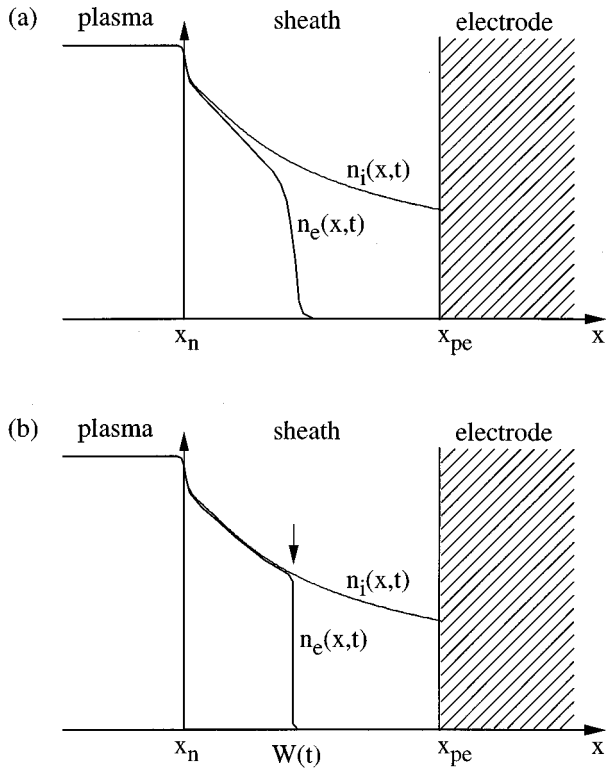

FIG. 1. (a) Cross section of the sheath along the x direction, perpendicular to the electrode. The electrode surface is on the right, at $x=x_{\mathrm{pe}}$. The plasma is on the left, with $x=x_n$ being an arbitrary position on the plasma side of the sheath. (b) Oscillating-step approximation for the electron density $n_e(x,t)$.

where $u_i(x,t)$ is the mean ion drift velocity directed toward the electrode. The ion collision term in Eq. (2) has been omitted, because, for high-density argon discharges, the mean free path of Ar^+ (3–6 mm at 1.33 Pa, calculated using a momentum transfer cross section [40] of $10^{-14}\,\mathrm{cm}^2$ and gas temperatures of 300–600 K) is large compared to the sheath width (which varies from ~0.1 mm with no rf bias to ~2 mm at hundreds of volts of rf bias). The ion diffusion term has been neglected in Eq. (2), because the ion drift velocity in the sheath is much greater than ion thermal velocities. Also, Eq. (3) omits the ionization and recombination terms.

Most previous sheath models [9–27] also omit the $\partial u_i/\partial t$ term in Eq. (2) and the $\partial n_i/\partial t$ term in Eq. (3). In high-frequency sheath models [9–19], these time-derivative terms are dropped, and E in Eq. (2) is replaced by the time-averaged electric field. These simplifications are valid in the limit $\omega/\omega_i \gg 1$, where $\omega=2\pi f$, f is the rf bias frequency, and ω_i is the ion plasma frequency, $\omega_i^2=n_i e^2/m_i\varepsilon_0$. In low-frequency sheath models [19–22], valid for $\omega/\omega_i \ll 1$, the time-derivative terms are dropped, but the time-dependent electric field is retained. In the model presented here, all time dependences are retained, so that the model is valid over the entire range of ω_i, from $\omega/\omega_i \ll 1$ to $\omega/\omega_i \gg 1$.

In contrast, because the electron mass m_e is small, the electron plasma frequency $\omega_e=n_e e^2/m_e\varepsilon_0$ is much higher than ω, and the electrons can be considered to respond instantaneously, without inertia, to the applied electric field. Assuming that the electrons have a Maxwell-Boltzmann velocity distribution with time-independent temperature T_e,

$$n_e(x,t)=n_{e0}\exp[eV(x,t)/kT_e], \tag{4}$$

where n_{e0} is the electron density at the center of the plasma and k is Boltzmann's constant.

The total current I_t is the sum of the ion current I_i the electron current I_e, and the displacement current I_d:

$$I_t(t)=I_i(x,t)+I_e(x,t)+I_d(x,t). \tag{5}$$

The currents I_i, I_e, and I_d vary with position, but I_t does not. We define the direction of positive current flow to be the direction from the electrode into the plasma, as in most experimental studies. Therefore, the ion current is

$$I_i(x,t)=-e\,n_i(x,t)\,u_i(x,t)A, \tag{6}$$

and the displacement current is

$$I_d(x,t)=-\varepsilon_0 A\,\partial E(x,t)/\partial t, \tag{7}$$

where A is the area of the electrode. The electron current at the electrode is

$$I_e(x_{\mathrm{pe}},t)=e\,A\,n_{e0}(eT_e/2\pi m_e)^{1/2}\exp[eV(x_{\mathrm{pe}},t)/kT_e]. \tag{8}$$

Here, and in Eq. (4), we have assumed that no electrons are emitted from the electrode.

A. Oscillating-step approximation

To solve Eqs. (1)–(8), one must know the boundary conditions on the plasma side of the sheath, i.e., at $x=x_n$. For a dc sheath, Bohm's theory [41] provides suitable boundary conditions. For rf sheaths in the high-frequency ($\omega/\omega_i \gg 1$) limit, Gierling and Riemann [18] provide a rigorous derivation of the boundary conditions. Unfortunately, it is not obvious how to apply their analysis at $\omega/\omega_i \approx 1$. Also, even at $\omega/\omega_i \gg 1$, their approach requires an inefficient iterative solution. At each time step, one or more of the boundary conditions must be adjusted repeatedly until one obtains the right value for the voltage drop across the sheath.

One way to avoid these problems is provided by oscillating-step models [9–15]. These models assume that the electron density profile consists of a sharp, steplike drop, which occurs at a time-varying position $W(t)$ shown in Fig. 1(b). On the plasma side of the step, $n_e=n_i$; on the sheath side, $n_e=0$. Therefore, Eq. (4) is replaced by

$$n_e(x,t)=\begin{cases} n_i(x,t), & x<W(t) \\ 0, & x\geqslant W(t) \end{cases}. \tag{9}$$

and Eq. (1) becomes

$$-\frac{\partial^2 V}{\partial x^2}=\frac{\partial E}{\partial x}=\begin{cases} 0, & x<W(t) \\ en_i(x,t)/\varepsilon_0, & x\geqslant W(t) \end{cases}. \tag{10}$$

At each time step, $W(t)$ is obtained very efficiently by numerically integrating Eq. (10), starting at the electrode, until the appropriate value is obtained for the voltage drop across the sheath. By introducing the time-varying width $W(t)$ to account for changes in sheath voltage, one avoids the need to vary the boundary conditions at x_n. One may instead use

time-independent boundary conditions, saving a lot of computation that would otherwise be spent adjusting them iteratively. Additional savings are obtained because the evaluation of the exponential function in Eq. (4) is avoided. The electron current is still calculated by Eq. (8), but that exponential is evaluated only at x_{pe}, not at every grid point.

The values of the boundary conditions at x_n differ from one step model to another. Here, the boundary conditions are chosen so that, for a dc sheath, the step model gives values of E, V, u_i, and n_i *at the electrode* that agree with Bohm's theory [41], which uses the more realistic electron density given in Eq. (4). Using this approach, as described in Appendix A, we obtain

$$E(x_n)=0, \tag{11}$$

$$V(x_n)=2kT_e/e, \tag{12}$$

$$u_i(x_n)=2(kT_e/m_i)^{1/2}, \tag{13}$$

and

$$n_i(x_n)=-I_0/eu_i(x_n)A, \tag{14}$$

where I_0 is the ion current flowing through the sheath, averaged over 1 rf cycle.

These boundary conditions differ from Bohm's boundary conditions. The ion velocity in Eq. (13), for example, is twice the Bohm velocity $u_B \equiv (kT_e/m_i)^{1/2}$. This apparent contradiction arises because we match the Bohm theory at the electrode, not at the plasma/sheath boundary. To get the ion velocity and energy at the electrode to agree with the Bohm theory, the step model must include the energy, of order kT_e, that ions gain between the Bohm point ($x=x_B$, where $u_i=u_B$ and $n_e \approx n_i$) and the point a few Debye lengths downstream where $n_e \approx 0$. In the step model, the transition from $n_e \approx n_i$ to $n_e \approx 0$ occurs discontinuously, rather than gradually over a few Debye lengths. Thus, in the step model, the only way to include the energy and velocity gained by ions crossing the Debye layer is to include them in the boundary condition at x_n. (See Appendix A.)

It might be argued that the values of the boundary conditions in Eqs. (11)–(14), derived for a dc sheath, do not apply to rf sheaths. Nevertheless, using these values, we obtain good agreement with experiment, better than that obtained using the values recommended by other step models. The results we obtain for rf sheaths also agree well with more detailed calculations that use the electron density given in Eq. (4) rather than the oscillating-step approximation of Eq. (9).

B. Method of solution

The model is solved numerically, by replacing the partial differential equations by finite difference equations. The region from x_n to x_{pe}, typically 0.2–2 mm thick, is represented by a grid of 50 points. The time step is chosen so that 2000 time steps fall within the rf period at 1 and 10 MHz, and 20 000 at 100 kHz.

At each time step, $W(t)$ is determined by numerically integrating the ion density in Eq. (10), starting at the electrode, until the appropriate value is obtained for the voltage drop across the sheath. We allow $W(t)$ to fall between grid points, by assuming that n_i varies linearly between grid points. Once $W(t)$ is known, the electric field is calculated at all grid points using Eq. (10). Then the currents in Eqs. (5)–(8) are calculated. Ion velocities are then updated using Eq. (2). Finally, ion densities are updated using Eq. (3).

Initially, the ion density and velocity are assumed to be constant in space, but they rapidly converge on a solution within a simulated time comparable to the time it takes ions to cross the sheath, about 100 ns. Solutions can be obtained in as little as 1 s of real time on an inexpensive microcomputer. Such speed, obtained due to the efficiency of the oscillating-step approximation, is needed if the model is to be used to analyze electrical signals as fast as they are acquired, for real-time process monitoring and control.

TABLE I. Parameters describing the experimental conditions of Ref. [32], where f is the rf bias frequency, P_L is the power applied to the inductive source, I_0 is the total time-averaged ion current at the rf-biased electrode, n_{e0} is the electron density prefactor in the electron current equation Eq. (8), and $\omega/\omega_i(x_B)$ is the ratio of the angular rf bias frequency $\omega=2\pi f$ to the ion plasma frequency at the Bohm point $\omega_i(x_B)$. Values of I_0 and n_{e0} are input to the model, along with the measured sheath voltage $V_{ps}(t)$ and the measured value for the effective electron temperature for high-energy electrons, $T_e=3.0$ eV.

f (MHz)	P_L (W)	$-I_0$ (A)	n_{e0} (10^{11} cm^{-3})	$\omega/\omega_i(x_B)$
0.1	350	1.031	4.20	0.006
0.1	120	0.319	1.25	0.010
0.1	60	0.105	0.29	0.017
1.0	350	1.038	4.20	0.055
1.0	120	0.319	1.25	0.099
1.0	60	0.104	0.29	0.174
10	350	1.029	4.20	0.56
10	120	0.319	1.25	1.01
10	60	0.103	0.29	1.78

C. Model input parameters

To solve the model, one must know the voltage across the sheath, i.e., $V(x_{pe},t)$; the time-averaged ion current I_0; the electron density at the center of the plasma n_{e0}; and the electron temperature T_e. Values of these parameters, and resulting values of ω/ω_i, are given in Table I. All the parameters were determined from measurements performed in previous studies. Measurements of the sheath voltage, denoted $V_{ps}(t)$, were obtained in Ref. [32]. Also in Ref. [32], I_0 was measured by applying a negative dc bias to the electrode sufficient to repel all plasma electrons.

Values for T_e and n_{e0} were obtained from Langmuir probe measurements [36] of the electron energy distribution function (EEDF). For high-density Ar discharges at 1.33 Pa [36] and 2.67 Pa [35] the EEDF is not Maxwellian. For these non-Maxwellian EEDFs, the electron current at the electrode can be calculated by first converting the measured EEDF $F(E)$ to the electron velocity distribution function $f(u)$, using

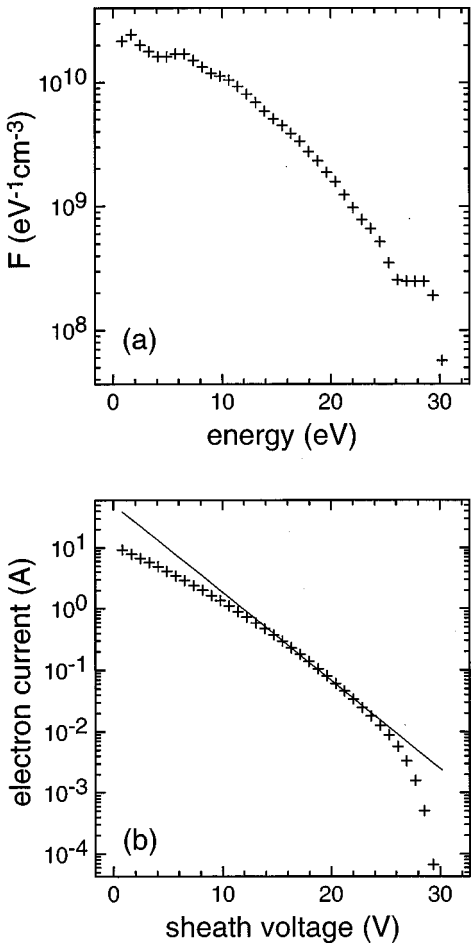

FIG. 2. (a) Electron energy distribution function measured in Ref. [36], using equipment and procedures described in Ref. [35], for a 1.33 Pa (10 mTorr) argon discharge at an inductive source power of 100 W, with no rf bias. (b) Electron current at the rf-biased electrode as a function of the sheath voltage calculated from the data in (a) using Eqs. (15)–(17). An exponential fit to the data (solid line) performed over the most important range of sheath voltage, from 14 to 22 V, gives an effective electron temperature of 3.0 eV.

$$F(E)dE = f(u)4\pi u^2\, du, \tag{15}$$

and then integrating,

$$I_e(t) = eA\int_{u_m}^{\infty}\int_0^{\infty}\int_0^{\infty} u_x f(u)\, du_x\, du_y\, du_z. \tag{16}$$

Here, u_x, u_y, and u_z are the three components of electron velocity, u is the magnitude of the electron velocity, and u_m, the lower limit of the integral over du_x, is given by

$$u_m = [-2eV_{\rm ps}(t)/m_e]^{1/2}. \tag{17}$$

Performing this analysis on the EEDF shown in Fig. 2(a), we obtain the electron current curve shown in Fig. 2(b). The most important part of $F(E)$ lies between ~14 and ~22 eV. Electrons below ~14 eV cannot cross the sheath, so they contribute no current; electrons above ~22 eV have such low densities that they contribute little current. Over the corresponding range of sheath voltages, 14–22 V, exponential

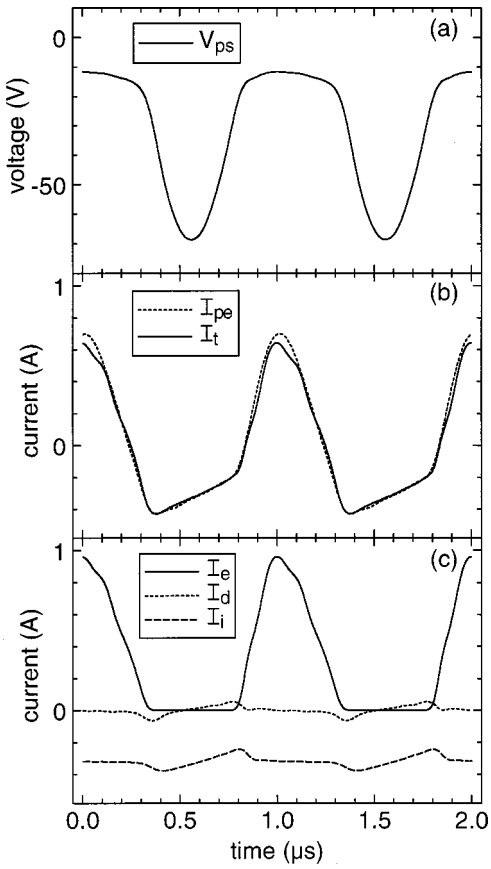

FIG. 3. Results of the numerical model compared to measurements, at 1 MHz rf bias frequency and an inductive source power of 120 W [i.e., at $\omega/\omega_i(x_B) = 0.10$]. (a) Measured sheath voltage $V_{\rm ps}(t)$. (b) Measured total current $I_{\rm pe}(t)$, and model total current $I_t(t)$. (c) Model electron current $I_e(t)$, ion current $I_i(t)$, and displacement current $I_d(t)$, all at the electrode surface.

fits of the data in Fig. 2(b) (and data taken at other inductive source powers) give an effective electron temperature of $kT_e = 3.0 \pm 0.1$ eV. Using this value of T_e, we then choose n_{e0} to give agreement with measured values of the floating potential, i.e., the voltage on the electrode when no rf bias is applied. By setting T_e and n_{e0} in this manner, we assure that the Maxwellian EEDF used by the model accurately reproduces the most important features of the measured, non-Maxwellian EEDF.

Finally, we also make use of the rf current at the electrode, $I_{\rm pe}(t)$, measured in Ref. [32]. The current is not a model input parameter; rather, it is an output of the model. Comparison of the model current to the measured current, in Secs. III A–III C, provides a rigorous test of the model. Then, in Secs. III D and III E, values of the impedance, phase, and power calculated from the measured current and voltage are compared to those predicted by the model.

III. RESULTS

A. Current wave forms at 1 MHz

Figure 3 shows measured current and voltage wave forms and the corresponding model wave forms, for a bias frequency of 1 MHz [$\omega/\omega_i(x_B) = 0.1$]. Figure 3(a) shows the measured sheath voltage $V_{\rm ps}(t)$. In Fig. 3(b), the measured

current $I_{pe}(t)$ is compared to $I_t(t)$, the total current predicted by the model. Overall, the agreement is excellent. The only noticeable difference between $I_{pe}(t)$ and $I_t(t)$ occurs near their maxima. This deviation is explained by the sensitivity of the model results to small errors in the model input parameters. In particular, the electron current $I_e(t)$ in Eq. (8) depends exponentially on $V_{ps}(t)$ and the electron temperature T_e. When $V_{ps}(t)$ in Fig. 3(a) is close to zero, and $I_e(t)$, shown in Fig. 3(c), is large, a small error in $V_{ps}(t)$ or T_e produces a larger error in $I_e(t)$, and hence in $I_t(t)$ as well. Propagating the uncertainty in the measurements [± 0.5 V in $V_{ps}(t)$ and ± 0.1 eV in kT_e] through the model calculations, one finds that the uncertainties are large enough to account for the deviation seen in Fig. 3(b).

In contrast, at times when the sheath voltage in Fig. 3(a) is strongly negative, the electron current in Fig. 3(b) is negligible. During this portion of the rf cycle, the ion current and the displacement current, $I_i(t)$ and $I_d(t)$, add together to produce an $I_t(t)$ wave form that is roughly linear with time. The model accurately predicts the slope and intercept of this linear section of the wave form.

The time dependence of the ion current, clearly shown in Fig. 3(c), is a very general effect that follows directly from the conservation of ions, Eq. (3). Nevertheless, only a few sheath models [28–30] try to account for it. Most models [9–27] instead assume that the ion current and flux are constant. Consequently, such models disagree with experiment and with the model presented here. For example, results from the Metze-Ernie-Oskam (MEO) model [23] are shown in Fig. 4. The displacement current predicted by the MEO model, shown in Fig. 4(c), is very similar to Fig. 3(c), but the constant ion current assumed by the MEO model differs from the time-dependent ion current in Fig. 3(c). Consequently, the total current predicted by the MEO model, $I_{MEO}(t)$, diverges from the measured current in Fig. 4(b) during the part of the rf cycle when the ion current is varying, i.e., from 0.3 to 0.8 μs. The electron currents in Figs. 4(c) and 3(c) also differ. Consequently, during the part of the cycle when the electron current is dominant, from 0.8 to 1.3 μs, $I_{MEO}(t)$ in Fig. 4(b) differs from the measured current more noticeably than $I_t(t)$ does in Fig. 3(b). The differences in $I_e(t)$ arise because the MEO model does not account for the non-Maxwellian EEDF. They can be avoided if the MEO model is modified so that T_e, n_{e0}, and I_0 are treated as independent parameters, as in the numeric model.

The Metze-Ernie-Oskam model has one advantage: it is simple enough to be solved analytically, rather than numerically. By taking an approach similar to Metze, Ernie, and Oskam—but being careful not to violate the conservation of ions—the numerical model presented here can be simplified to yield an analytic model. This analytic model is derived in Appendix B. Predictions of the model are shown in Fig. 5. The agreement with the experimental current wave form in Fig. 5(b) is nearly as good as that obtained with the numerical model in Fig. 3(b). Furthermore, the electron, ion, and displacement currents from the analytic model in Fig. 5(c) are all quite similar or identical to the corresponding numerical results in Fig. 3(c). Thus, for many purposes, at the rf bias frequency of 1 MHz [e.g., at $\omega/\omega_i(x_B)=0.1$], the analytic model may be used instead of the numerical model,

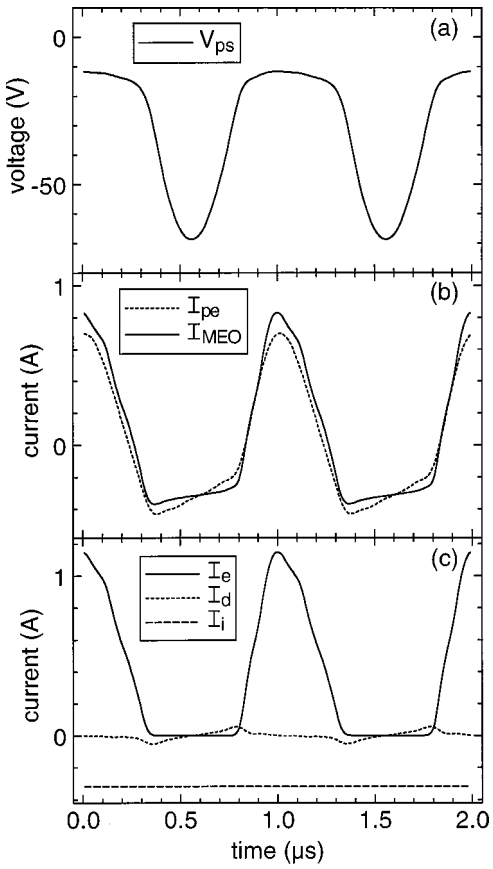

FIG. 4. Comparison of the Metze-Ernie-Oskam model [23] to experimental data at 1 MHz. (a) Measured sheath voltage $V_{ps}(t)$. (b) Measured total current $I_{pe}(t)$ and model total current $I_{MEO}(t)$. (c) Model electron current $I_e(t)$, ion current $I_i(t)$, and displacement current $I_d(t)$, all at the electrode surface. The data are the same as in Fig. 3. Model results were calculated using $I_0 = -0.319$ A and $kT_e = 3.0$ eV.

with little loss of accuracy and a significant savings in computation.

The analytic model explains why the shapes of the displacement current and the ion current are similar in Fig. 5(c) [and also in Fig. 3(c)]. Both contain a factor of dV_{ps}/dt, the derivative of the sheath voltage. The analytic model also explains why, in previous work [32], better agreement with 1 MHz data was obtained by arbitrarily increasing the displacement current in the Metze-Ernie-Oskam model by a factor of 3. Scaling up the displacement current compensates for the missing time-dependent ion current.

Also, notice in Figs. 3(c) and 5(c) that the peak-to-peak amplitude of the ion current is larger than that of the displacement current. The equations of the analytic model, Eqs. (B8) and (B10) predict that the time-dependent part of the ion current will always be larger than the displacement current, no matter how low the frequency (i.e., no matter how small the derivative dV_{ps}/dt). Thus, there is no frequency regime where the MEO predictions are valid, that is, where the displacement current at the electrode is significant but the time dependence of the ion current at the electrode is not significant.

The time dependence of the ion current arises because ions entering the sheath at different times experience different electric fields, and therefore take different amounts of

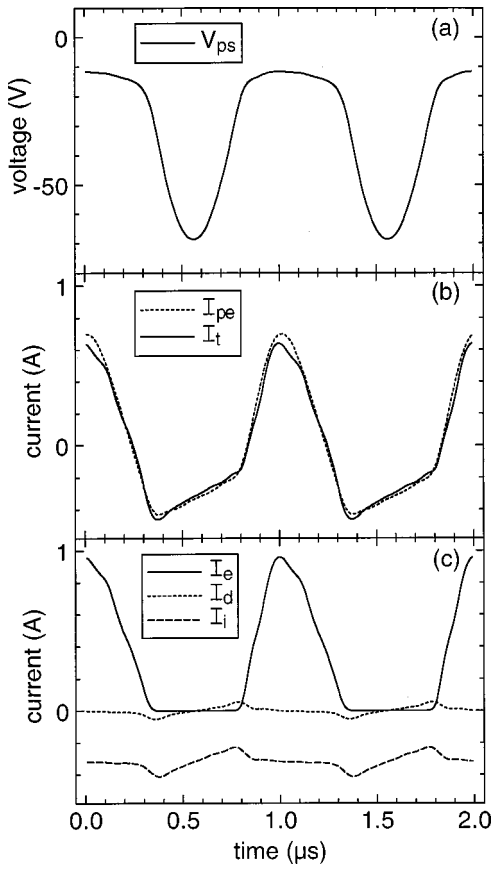

FIG. 5. Comparison of the analytic model (derived in Appendix B) to experimental data. (a) Measured sheath voltage $V_{ps}(t)$. (b) Measured total current $I_{pe}(t)$ and model total current $I_t(t)$. (c) Model electron current $I_e(t)$, ion current $I_i(t)$, and displacement current $I_d(t)$, all at the electrode surface. The conditions are the same as in Fig. 3.

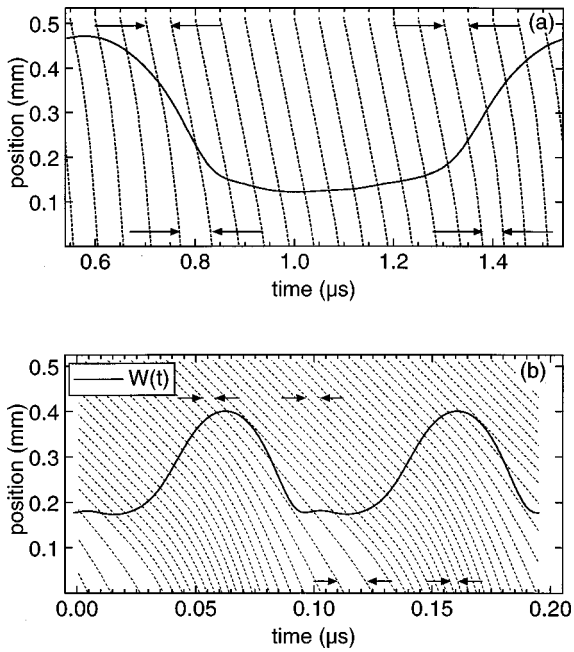

FIG. 6. Ion trajectories (dotted lines) and the sheath width $W(t)$ (solid line) at rf bias frequencies of (a) 1 and (b) 10 MHz. The surface of the electrode is on the bottom axis, at position 0; the plasma extends above the top axis. The trajectories are evenly spaced far from the electrode, but not near the electrode, as indicated by the arrows. For (a) the conditions and the time scale are the same as in Fig. 3.

time to cross the sheath. The variation in ion transit time means that there must be times in the rf cycle when more ions than average arrive at the electrode and times when fewer arrive. To illustrate this effect, ion trajectories for the 1 MHz simulations of Fig. 3 are shown in Fig. 6(a). [The effect is even more visible in Fig. 6(b), at 10 MHz.] Examining Fig. 6(a), one sees, for example, that ions beginning at a position 0.5 mm from the electrode at time 0.700 μs reach the electrode at time 0.771 μs, but ions starting later, at time 0.750 μs (when the sheath voltage is less negative, the sheath width smaller, and the electric field weaker) take longer, arriving at the electrode at time 0.835 μs. This means that all ions starting at 0.5 mm between 0.700 and 0.750 μs—50 ns worth of ion flux—arrive at the electrode staggered over a longer time interval of length 64 ns. Therefore, during this interval, the magnitude of the ion current and flux at the electrode must be decreased by a factor of 50/64 from the current and flux at position 0.5 mm. [Referring back to Fig. 3(c), one sees that the magnitude of the ion current near 0.8 μs is indeed reduced by this factor relative to its time-averaged value.) On the other hand, during the portion of the rf cycle near 1.4 μs in Fig. 6(a)—when the sheath voltage is becoming more negative, the sheath width is increasing, and the electric field is becoming stronger—ions entering the sheath have shorter transit times than the ions immediately preceding them. Thus an interval of flux arrives at the electrode compressed into a shorter time period, and the magnitude of the ion current at the electrode is increased, as seen in Fig. 3(c). Finally, for portions of the cycle near 1.1 μs, when the sheath voltage and sheath width are more or less constant, the transit times of successive ions are also constant, and thus the ion flux and current are constant in time.

For a more rigorous treatment of these effects, see Appendix C. There, we derive a general relation that expresses the dependence of the ion current on ion transit time.

B. Current wave forms at 100 kHz

Figure 7 shows measured current and voltage wave forms and the corresponding model wave forms, for a bias frequency of 100 kHz. In Fig. 7(b), the agreement between the measured current wave form $I_{pe}(t)$ and the total current predicted by the model, $I_t(t)$, is good, although $I_t(t)$ again deviates from $I_{pe}(t)$ at times when the sheath voltage [$V_{ps}(t)$, shown in Fig. 7(a)] is close to zero and the electron current [$I_e(t)$ in Fig. 7(c)] is large. Again, this deviation is explained by the sensitivity of the calculated electron current to small errors in $V_{ps}(t)$ and T_e, as discussed above. Also, near their maxima, ringing is observed in $I_t(t)$ and $I_e(t)$. This ringing results from a small ringing present in the sheath voltage [shown magnified in Fig. 7(a)], which in turn is an artifact of the Fourier analysis procedures used in Ref. [32] to obtain $V_{ps}(t)$ from digitized wave forms. These procedures [42,43] enable us to account for the effects of stray impedance, propagation delays, and probe errors, to filter noise, and to interpolate between the digitized points. Unfortunately, applying Fourier techniques to wave forms with sharp peaks or corners usually results in some amount of ringing.

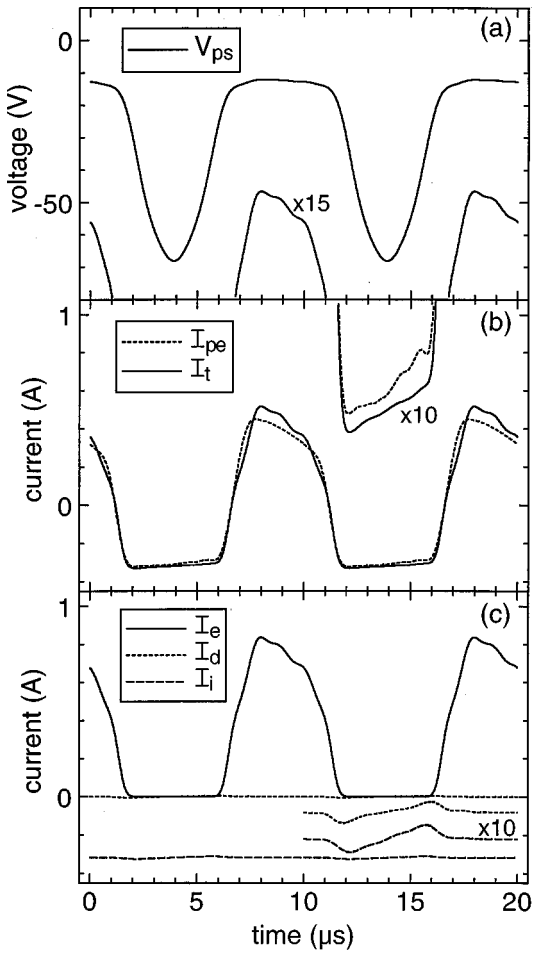

FIG. 7. Results of the numerical model compared to measurements, at 0.1 MHz rf bias frequency and an inductive source power of 120 W [i.e., at $\omega/\omega_i(x_B)=0.01$]. (a) Measured sheath voltage $V_{ps}(t)$. (b) Measured total current $I_{pe}(t)$ and model total current $I_t(t)$. (c) Model electron current $I_e(t)$, ion current $I_i(t)$, and displacement current $I_d(t)$, all at the electrode surface. Selected portions of the wave forms have been magnified in the vertical direction by the indicated factors (and shifted vertically by arbitrary amounts).

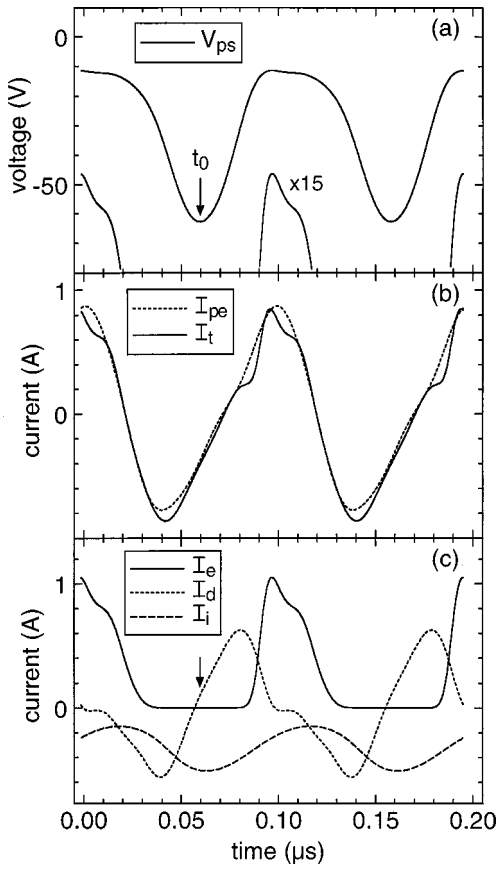

FIG. 8. Results of the numerical model compared to measurements, at 10 MHz rf bias frequency and an inductive source power of 120 W [i.e., at $\omega/\omega_i(x_B)=1.0$]. (a) Measured sheath voltage $V_{ps}(t)$, shown normal size and magnified 15× in the vertical direction. (b) Measured total current $I_{pe}(t)$ and model total current $I_t(t)$. (c) Model electron current $I_e(t)$, ion current $I_i(t)$, and displacement current $I_d(t)$, all at the electrode surface. Arrows indicate that at time t_0, when $V_{ps}(t)$ is minimized, $I_d \neq 0$.

Near their minima, $I_{pe}(t)$ and $I_t(t)$ in Fig. 7(b) look rather flat. Nevertheless, the magnified view in Fig. 7(b) shows that they actually have positive slopes, which are generally in agreement. (Some ringing is observed in the magnified plot of $I_{pe}(t)$, for the reasons discussed above.) Similarly, the displacement current $I_d(t)$ and ion current $I_i(t)$ in Fig. 7(c) at first appear to be constant, but when they are magnified they are seen to have shapes similar to that seen at 1 MHz, in Fig. 3(c). The MEO model [23] predicts a similar $I_d(t)$ wave form, but assumes constant ion current, thereby underestimating the slope of the total current. Of course, this slope is a relatively minor feature, so that, for many purposes, the MEO model may be adequate at 100 kHz [i.e., at $\omega/\omega_i(x_B)=0.01$]. Indeed, even simpler models [19–22], which neglect the displacement current as well as the time dependence of the ion current, may be adequate.

The modulation in ion current at 100 kHz, in Fig. 7(c), is ten times smaller than that at 1 MHz, in Fig. 3(c). This result is predicted by the analytic model, since the derivative of the sheath voltage in Eq. (B10) is ten times smaller at 100 kHz than at 1 MHz. [Except for the tenfold difference in time scale, the sheath voltages in Figs. 3(a) and 7(a) are nearly identical.] This result can also be explained by Eq. (C3). In Figs. 7 and 3, ion transit times vary over the same range and in the same manner. Nevertheless, at 100 kHz, the variations occur on a time scale ten times longer, so the derivative of transit time in Eq. (C3) is ten times smaller, as is the time-dependent part of the ion current. Conversely, by increasing the rf frequency above 1 MHz, the modulation in ion current become larger, as shown in the next section.

C. Current wave forms at 10 MHz

Current and voltage wave forms measured at 10 MHz rf bias frequency, and the corresponding model wave forms, are shown in Fig. 8. As discussed above, when the sheath voltage $V_{ps}(t)$ shown in Fig. 8(a) is close to zero, the electron current in Fig. 8(c) becomes large, and it becomes especially sensitive to uncertainties in $V_{ps}(t)$ and T_e, causing the model current $I_t(t)$ in Fig. 8(b) to deviate from the measured current $I_{pe}(t)$. The deviation on the shoulder of the current wave forms, at 0.085 μs, may also be related to errors in $V_{ps}(t)$. In addition, we also see a deviation at 0.04 μs, near the minima of the current wave forms, which is ob-

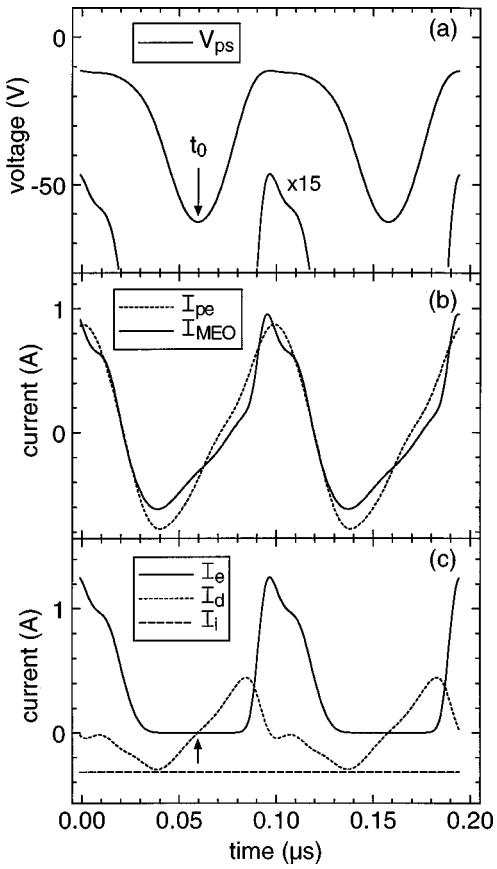

FIG. 9. Comparison of the Metze-Ernie-Oskam model [23] to experimental data at 10 MHz. (a) Measured sheath voltage $V_{ps}(t)$, shown normal size and magnified 15×. (b) Measured total current $I_{pe}(t)$ and model total current $I_{MEO}(t)$. (c) Model electron current $I_e(t)$, ion current $I_i(t)$, and displacement current $I_d(t)$, all at the electrode surface. Arrows show that $I_d=0$ at time t_0, when $V_{ps}(t)$ is minimized. The data are the same as in Fig. 8. Model results were calculated using $I_0=-0.319$ A and $kT_e=3.0$ eV.

served consistently at 10 MHz and sometimes at 1 MHz. Possible explanations for this deviation are discussed below in Sec. IV.

Predictions of the Metze-Ernie-Oskam model at 10 MHz are shown in Fig. 9. In Fig. 9(b), the agreement with experiment is worse than that seen in Fig. 8(b), for several reasons. First, the ion current is constant in the MEO model. Second, the electron current does not account for the non-Maxwellian EEDF, as discussed above. Third, the MEO model also gets the displacement current wrong. The displacement current $I_d(t)$ depends on the ion density profile $n_i(x,t)$ as well as the sheath voltage. The MEO model assumes that, in the reference frame moving with the sheath edge, $n_i(x,t)$ does not vary with time. This assumption is reasonable for lower frequencies, but not at 10 MHz [i.e., at $\omega/\omega_i(x_B)=1.0$]. The analytic model derived in Appendix B also makes this assumption, so it also has significant errors at 10 MHz in $n_i(x,t)$ and $I_d(t)$, as well as $I_i(t)$.

The disagreement between the MEO model and experiment seen in Fig. 9(a) suggests that serious misinterpretations may arise when the MEO or similar models are used to interpret measured wave forms and extract plasma parameters. In particular, consider the method of Ref. [6], which is illustrated in Fig. 9. At the time t_0 when the sheath voltage reaches its minimum, the MEO model—and other models based on Eq. (B8) or similar equations—predict that the displacement current will be zero. Furthermore, if the minimum is far enough negative, the electron current will also be zero. Therefore, simply by taking the total current at t_0, one obtains a value for the ion current. One problem with this technique is that, according to the complete numerical model, I_d is not necessarily zero at time t_0 [see Fig. 8(c)]. Also, because the ion current varies with time, the estimate of the ion current obtained at t_0 need not agree with the time-averaged ion current I_0. Thus, in Fig. 9, $I_{pe}(t_0)=-0.377$ A, whereas $I_0=-0.319$ A. At other conditions, shown in Fig. 10, $I_{pe}(t_0)$ differs from I_0, sometimes by more than 60%. In contrast, the total current at time t_0 predicted by the complete numeric model, also shown in Fig. 10, agrees much better with $I_{pe}(t_0)$. This suggests that, by fitting the complete model to measured current and voltage wave forms, values for the time-averaged ion current can be obtained that are more accurate than those given by Ref. [6].

The ion current in Fig. 8(c) shows a larger amplitude modulation than that seen at 1 MHz in Fig. 3(c). At 10 MHz, variations in transit time occur over a shorter time scale than at 1 MHz, so the derivative in Eq. (C3) is larger at 10 MHz, as are the oscillations in $I_i(t)$. Nevertheless, at 10 MHz, a competing effect is beginning to become important. As

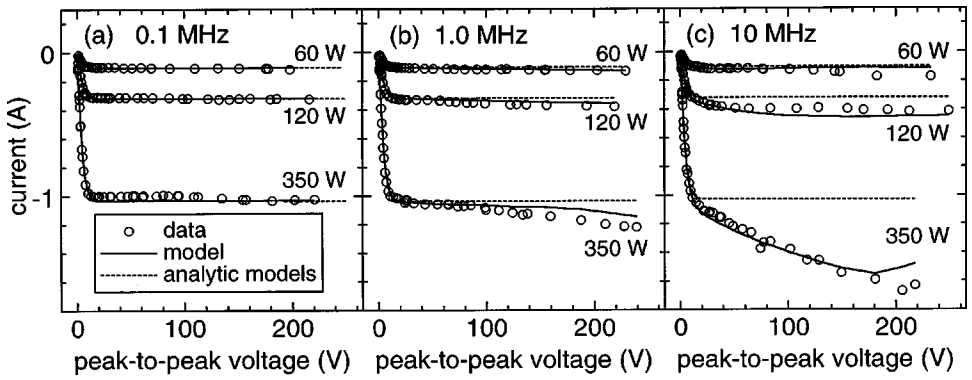

FIG. 10. Values of the total current at t_0, the time of the voltage minimum, for rf bias at (a) 0.1, (b) 1.0, and (c) 10 MHz, inductive source powers of 60, 120, and 350 W, and varying rf bias amplitudes, indicated on the x axis by the peak-to-peak amplitude of the sheath voltage $V_{ps}(t)$. Symbols (○) indicate the measured current $I_{pe}(t_0)$; solid lines indicate the model total current $I_t(t_0)$; dotted lines indicate the total current from analytic models such as the Metze-Ernie-Oskam model.

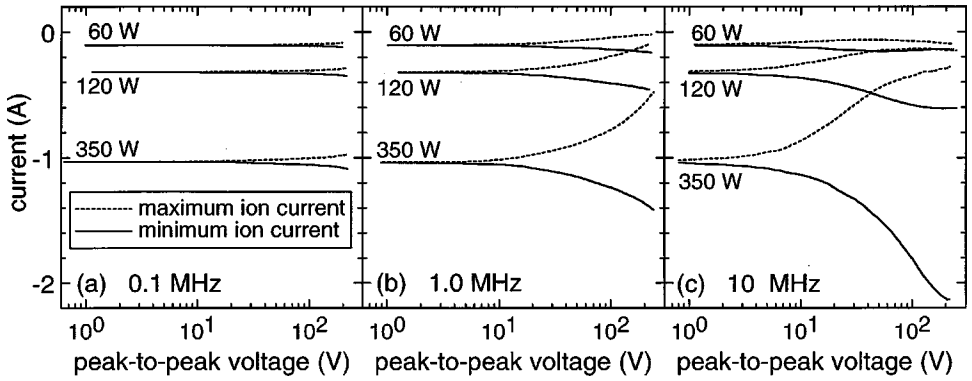

FIG. 11. Value of the minimum (solid lines) and maximum (dotted lines) ion current predicted by the numerical model for rf bias at (a) 0.1, (b) 1.0, and (c) 10 MHz, and inductive source powers of 60, 120, and 350 W.

shown by the trajectories in Fig. 6(b), the ion transit times are a substantial fraction of the rf period at 10 MHz. Thus any ion, no matter when it enters the sheath, experiences a range of both higher- and lower-field portions of the rf cycle. Thus, the variations in electric field tend to average out, making the transit time less sensitive to the time that the ion entered. This effect makes the derivative in Eq. (C3) smaller, which makes the modulation in ion current smaller. Evidence of this effect can be seen in Fig. 11. There, we see that the modulation in ion current usually grows larger as the sheath voltage increases, but in Fig. 11(c), at an inductive source power of 60 W, the modulation instead begins to decrease with increasing sheath voltage, because of the averaging effect.

If the rf bias frequency is increased above 10 MHz, the transit times eventually become much longer than the rf period, the time variations in the electric field tend to entirely average out, the transit time of an ion becomes insensitive to its arrival time, and the time dependence of the ion current becomes negligible. Under such conditions, high-frequency sheath models [9–19] are valid. The model presented here predicts that the modulations of the ion current become small ($\pm 10\%$) at $\omega/\omega_i(x_B) \approx 3$. This agrees with previous work [15,31] on lower-density, capacitively coupled discharges, where good agreement with high-frequency models was obtained at $3.5 \leqslant \omega/\omega_i \leqslant 30$.

Figure 6 illustrates another effect. When the transit times are comparable to the rf period, as in Fig. 6(b), the dependence of transit time on phase differs from that seen at lower frequencies. Therefore, the phase of the ion current modulation also changes. Unlike Fig. 3(c) [and Eq. (B10)] where the modulation is in phase with the derivative of the voltage, in Fig. 8(c) it is in phase with the voltage. This change greatly affects the power absorbed by ions in the sheath, as described in Sect. III E below.

D. Impedance

Sheath impedances were calculated from the fundamental components (i.e., the components at the rf bias frequency) of the sheath voltage $V_{ps}(t)$, the measured current $I_{pe}(t)$, and the model current $I_t(t)$. Magnitudes of the measured and model sheath impedances are shown in Fig. 12. Figure 13 plots their phases. Rather good agreement is obtained over the entire data set, which covers two orders of magnitude in sheath voltage and rf bias frequency. The plots of the model results are not smooth curves because of errors in the model input parameters. As discussed above, small errors in the sheath voltage produce large errors in the electron current, which in turn show up in the impedance magnitude and phase. At worst, model values differ from the measurements by -11% and $+24\%$ in magnitude and $-12°$ and $+5°$ in

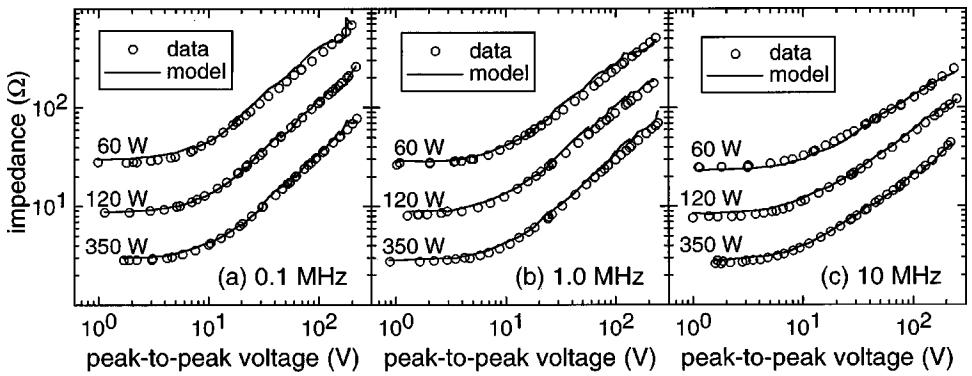

FIG. 12. Magnitudes of the measured and model sheath impedances at rf bias frequencies of (a) 0.1, (b) 1.0, and (c) 10 MHz, inductive source powers of 60, 120, and 350 W, and varying rf bias amplitudes, indicated on the x axis by the peak-to-peak amplitude of the sheath voltage $V_{ps}(t)$. The measured sheath impedances, i.e., the ratio of the fundamental components of $V_{ps}(t)$ and the measured current $[I_{pe}(t)]$, are shown as symbols (○). The model sheath impedance, i.e., the ratio of the fundamental components of $V_s(t)$ and the model current $[I_t(t)]$, are indicated by solid lines.

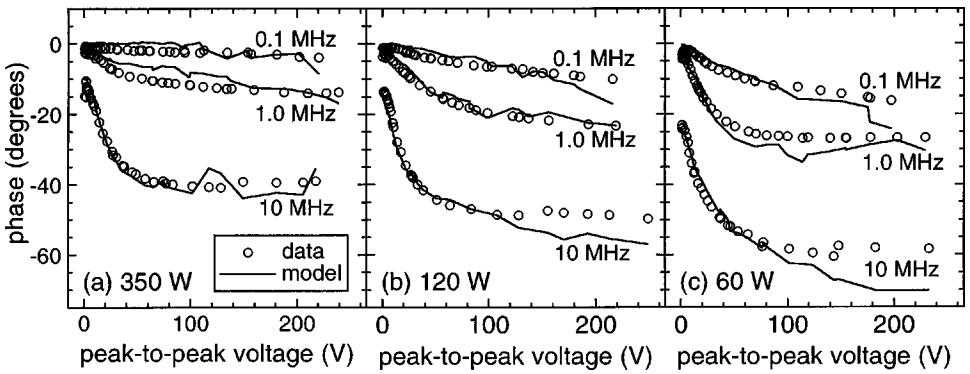

FIG. 13. Phases of the measured and model sheath impedances, defined in Fig. 12, at inductive source powers of (a) 350, (b) 120, and (c) 60 W, at rf bias frequencies of 0.1, 1, and 10 MHz, and varying rf bias amplitudes, indicated on the x axis by the peak-to-peak amplitude of the sheath voltage $V_{ps}(t)$. The measurements are shown as symbols (○). The model results are indicated by solid lines.

phase. These differences (except for the largest differences in phase, seen at high sheath voltages at 10 MHz) are within the combined uncertainties of the measurements (±6% and ±1°) and the model (obtained by propagating the uncertainties in model input parameters). Nevertheless, these comparisons may be somewhat misleading because the model uncertainty is contributed nearly entirely by the electron current. Thus, a significant deviation in ion current or displacement current may produce a deviation in the impedance that is deemed insignificant because of the large uncertainty in electron current. Results from the Metze-Ernie-Oskam model do not agree as well with the data. They differ by as much as −44% to +46% in magnitude and −14° to +17° in phase.

E. Power

We obtain the measured power P_{ps} and the model power P_t from

$$P_{ps} = \int_0^T I_{pe} V_{ps} dt, \tag{18}$$

and

$$P_t = \int_0^T I_t V_{ps} dt, \tag{19}$$

where T is the rf period. Values of P_{ps} and P_t, shown in Fig. 14, are in good agreement. A deviation is observed at high voltages at 10 MHz, but it is within the uncertainty of the measurements (±8%) and the uncertainty in the model (±6% for the high-voltage, 10 MHz data, obtained by propagating the uncertainty in the model input parameters).

For the Metze-Ernie-Oskam model, and other analytic models, the power can be approximated by

$$P = I_0 (V_{ps0} - V_f), \tag{20}$$

where V_{ps0} is the dc voltage across the sheath, and V_f is the value of V_{ps0} when no rf bias is applied [32]. The first term is the power gained by ions as they are accelerated across the presheath and the sheath. The second term is a good approximation for the power lost by electrons, which are decelerated as they cross the sheath.

In Ref. [32] it was found that the analytic result Eq. (20) often disagreed with P_{ps} measurements. This can be seen in Fig. 14. At 100 kHz P_{ps} values fall on the dotted lines, which represent Eq. (20), but at 1 and 10 MHz P_{ps} values are higher by as much as 40%. The disagreement with Eq. (20) arises because its derivation assumes that the ion current is constant in time. If the ion current varies with time, the ions are able to absorb more power, especially at 10 MHz [i.e., at $\omega/\omega_i(x_B) = 1.0$], where the oscillation in ion current is large and in phase with the sheath voltage [see Figs. 8(a) and 8(c)].

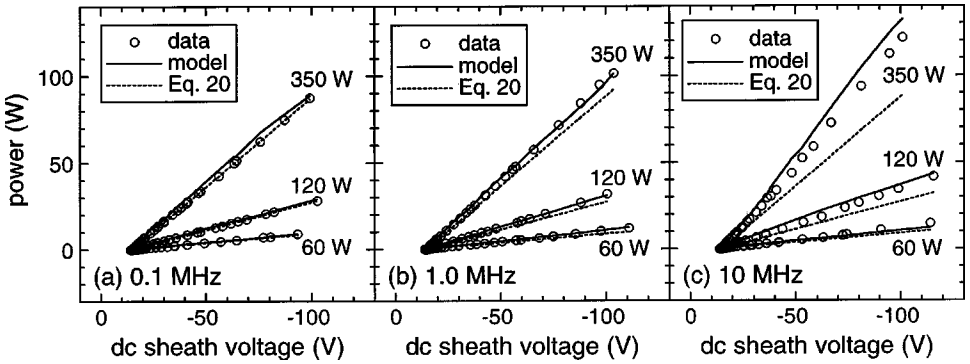

FIG. 14. Power dissipated in the sheath at rf bias frequencies of (a) 0.1, (b) 1.0, and (c) 10 MHz, at inductive source powers of 60, 120, and 350 W, and varying rf bias amplitudes, indicated on the x axis by the dc component of the sheath voltage $V_{ps}(t)$. Symbols (○) indicate the measured power P_{ps} from Eq. (18). Solid lines indicate the model power from Eq. (19). Dotted lines indicate the power predicted by analytic models given by Eq. (20).

This effect also explains the results presented in Ref. [25], where measured powers were found to be as much as 50% higher than the powers predicted by the Riley sheath model [25], which, like the analytic models, neglects the time dependence of the ion current. Other recent work [30] confirms this explanation. The failure of analytic or other models to accurately predict the power implies that their predictions for ion energy distributions will also be in error.

IV. DISCUSSION

Here we discuss extensions to the model and possible explanations for the disagreements between the model and the data, such as that shown in Fig. 8. One possible source of disagreement is the boundary conditions chosen in Eqs. (11)–(14). Simulations performed with different values of the boundary conditions, however, did not yield any better agreement with experiment. Also, very similar results were obtained by using the Boltzmann electron profile of Eq. (4) [with $n_e(x_n)$ adjusted iteratively at each time step to give the appropriate sheath voltage] rather than the oscillating step. Thus the oscillating-step approximation does not appear to be a major source of error.

Stochastic heating or other heating mechanisms for electrons are another possible source of disagreement. Absorption of rf bias power by these mechanisms is not included in the model, since the model uses values of T_e and n_{e0} measured with no rf bias applied. When rf bias is applied, however, changes are observed in time- and space-resolved optical emission measurements [37], which may suggest that some part of the rf bias power is indeed absorbed by electrons. The observed changes are small, on the order of a few percent of the total light emitted by the discharge. Thus the power absorbed by electrons is presumably small, but it may be important. Electrons heated at the sheath edge are accelerated into the plasma, but they may be reflected by elastic collisions with atoms or the opposing sheath, and thus reach the rf-biased electrode. Stochastic heating should be greater at higher frequencies, and at the time in the rf cycle when dV_{ps}/dt is large and negative, e.g., around $t=0.04\ \mu$s in Fig. 8. An increase in the electron current at that time would make the model total current $I_t(t)$ more positive, in better agreement with $I_{pe}(t)$. Changes in the EEDF due to electron heating could also affect the displacement current.

It is also possible for stochastic heating to produce an increase in ionization in the discharge, and thus an increase in the ion current. No increase in ion current during rf biasing has been observed, however, in Langmuir probe studies [25,36]. Furthermore, an increase in ion current would make the total model current $I_t(t)$ more negative, which would result in poorer agreement with $I_{pe}(t)$ in Fig. 8. Similarly, ionization within the sheath would increase the total ion charge in the sheath, making the displacement current stronger, which would result in worse, not better, agreement in Fig. 8.

The model neglects electron emission from the electrode surface. Nevertheless, by setting n_{e0} to give the measured floating potential, the current of any electron-induced secondaries is effectively included in $I_e(t)$. The yield of ion-induced secondaries should be small, because the ion energies are low ($\leqslant$250 eV). Furthermore, ion-induced secondaries would make the model current $I_t(t)$ more negative, which would result in poorer agreement with $I_{pe}(t)$ in Fig. 8. Nevertheless, because emitted electrons are accelerated so efficiently, heating mechanisms involving emitted electrons may need to be considered.

The effect of ion collisions was studied by including an ion drag term in Eq. (2). As noted previously [15], the effect of this term is to increase the ion charge in the sheath and thereby increase the amplitude of the displacement current. This increase yields worse, not better, agreement in Fig. 8. Nevertheless, if simulations of pressures considerably higher than 1.33 Pa (10 mTorr) are desired, collisions would need to be included. Also, to simulate discharges in reactive gases, the model would need to be extended to include more than just one positive ionic species. Negative ions are repelled by the sheath fields, so they need not be considered explicitly. They may, however, alter the boundary conditions at the plasma/sheath interface [44].

Langmuir probe studies [33,35] show that the ion and electron currents in the inductive GEC cell are not radially uniform. To study the effect of such nonuniformities, we performed simulations in which the electrode area was divided into discrete subregions with different current densities, given by Langmuir probe data. Results were remarkably similar to those of the radially uniform simulations presented above. Thus the nonuniformities are not large enough to appreciably affect the simulations.

Another possible extension of the model would be to include both sheaths in the simulation, as in Ref. [25]. In such an approach, the sheath voltage is no longer a model input parameter. Instead, the individual sheath voltages are determined by the model from their sum, the voltage on the electrode, which can be determined with less uncertainty. Thus the two-sheath approach would allow one to avoid the problems caused by the sensitivity of the electron current to errors in measured sheath voltage.

Finally, the model does not include very-high-frequency effects such as field reversal [45] or plasma-sheath series resonance [17]. These effects, related to electron inertia, should appear at frequencies above 100 MHz, beyond the range of interest here. Components at and near the series resonance frequency do not appear in the measured current wave forms, because they are filtered out by the measurement equipment and Fourier analysis procedures. Such components are at frequencies too high for Ar^+ ions to respond to, so they are of relatively little interest for the present study, although they may be more important for discharges in H_2, He, or other light gases.

V. CONCLUSIONS

The results presented here show how the electrical behavior of plasma sheaths depends on $\omega/\omega_i(x_B)$, the ratio of the rf bias frequency to the ion plasma frequency at the edge of the sheath. At $\omega/\omega_i(x_B)\leqslant 0.01$, the displacement current and time-dependent ion current are small. For such low frequencies, many models, even models [19–22] that neglect these currents entirely, agree reasonably well with experiment. As $\omega/\omega_i(x_B)$ increases to $\sim$0.1, the displacement current and time-dependent ion current become larger, and thus low-frequency models [19–22] become invalid. The Metze-

Ernie-Oskam model accurately predicts the displacement current at $\omega/\omega_i(x_B)=0.1$, but it neglects the time-dependent ion current, resulting in significant errors. In contrast, the numerical model presented here, as well as an analytic approximation for it, are in excellent agreement with measurements at $\omega/\omega_i(x_B)=0.1$. At $\omega/\omega_i(x_B)\approx 1$, both the displacement current and the ion current predicted by the Metze-Ernie-Oskam model have significant errors. The numerical model is still reasonably accurate at $\omega/\omega_i(x_B)\approx 1$, but the analytic approximation for the model is no longer valid. At $\omega/\omega_i(x_B)\approx 1$, the modulation in ion current is very large: in some cases, over the course of the rf cycle, the ion current ranges from as low as 20% to more than 200% of its time-averaged value. Values of the ion current obtained from models that neglect the modulation may consequently be in error by as much as 80–100 %. The modulation in ion current is in phase with the sheath voltage at $\omega/\omega_i(x_B)\approx 1$, which allows ions in the sheath to absorb as much as 40–50 % more power than at lower or higher frequencies (for the same sheath voltage). Models that neglect the modulation in ion current thus underestimate the power absorbed in the sheath by as much as 40–50 %. Finally, as $\omega/\omega_i(x_B)$ continues to increase above 1, the ion current modulation decreases, as ions become less able to respond to the rf fields. For $\omega/\omega_i(x_B)>3$, the time dependence of the ion current becomes small, and high-frequency sheath models [9–19] are valid.

The numeric model presented here gives good agreement over the whole range of $\omega/\omega_i(x_B)$. The implementation of the model, which uses the oscillating-step approximation, is numerically very efficient and thus it is well suited for analyzing electrical signals in real time. The good agreement obtained here suggests that important physical parameters like total ion current or flux and ion bombardment energies could be reliably obtained from measurements of rf electrical signals, interpreted using the model. Algorithms for obtaining such parameters are under development.

ACKNOWLEDGMENTS

I would like to thank Axel Schwabedissen for graciously providing Langmuir probe measurements of the electron distribution function, and James Whetstone for valuable discussions.

APPENDIX A: BOUNDARY CONDITIONS FOR THE OSCILLATING-STEP MODEL

Here, the boundary conditions for the step model are obtained by matching it to Bohm's dc sheath model [41], which includes a more realistic profile for the electron density. We start with the dc versions of Eqs. (2) and (3),

$$u_i\,\partial u_i/\partial x = eE/m_i \tag{A1}$$

and

$$\partial(n_i\,u_i)/\partial x = 0. \tag{A2}$$

We integrate these equations, starting at a point $x=x_B$ on the boundary between the plasma and the sheath, where $E(x_B)\approx 0$, $V(x_B)\equiv V_B$, $u_i(x_B)\equiv u_B$, and $n_e(x_B)\approx n_i(x_B)\equiv n_B$. We obtain

$$\tfrac{1}{2} m_i\,u_i(x)^2 = -eV(x), \tag{A3}$$

and

$$n_i(x)u_i(x) = n_B\,u_B = n_B\left(\frac{-2eV_B}{m_i}\right)^{1/2} = \frac{-I_0}{eA}. \tag{A4}$$

Substituting n_i from these equations and n_e from Eq. (4) into Eq. (1), we obtain

$$\varepsilon_0\frac{\partial^2 V}{\partial x^2} = -e\,n_B\left\{\left(\frac{V}{V_B}\right)^{-1/2} - \exp\left[\frac{e(V-V_B)}{kT_e}\right]\right\}. \tag{A5}$$

We integrate this equation over dV, using

$$\int \frac{\partial^2 V}{\partial x^2}\,dV = \int \frac{\partial^2 V}{\partial x^2}\frac{\partial V}{\partial x}\,dx = \int \frac{\partial E}{\partial x}E\,dx = \int E\,dE \tag{A6}$$

and obtain

$$\varepsilon_0 E^2 = 2n_B(2eV_B[(V/V_B)^{1/2}-1] + kT_e\{\exp[e(V-V_B)/kT_e]-1\}). \tag{A7}$$

Now we repeat this derivation using the step model, i.e., using Eq. (9) instead of Eq. (4). At the position $x=x_S$, where the steplike drop in electron density occurs, we have new boundary conditions $E(x_S)\approx 0$, $V(x_S)\equiv V_S$, $u_i(x_S)\equiv u_S$, $n_e(x_S)\approx 0$, and $n_i(x_S)\equiv n_S$. This time we get

$$\varepsilon_0 E^2 = 2n_S\{2eV_S[(V/V_S)^{1/2}-1]\}. \tag{A8}$$

We now match Eq. (A8) to Eq. (A7), noting that, for high voltages, $-V+V_B \gg kT_e$, the exponential term in Eq. (A7) can be ignored. The two equations are then equivalent if

$$V_S = V_B - kT_e/e + k^2T_e^2/(4e^2V_B). \tag{A9}$$

If

$$V_B = -kT_e/2e, \tag{A10}$$

the critical value derived by Bohm, then

$$V_S = -2kT_e/e, \tag{A11}$$

$$u_S = 2u_B = 2(kT_e/m_i)^{1/2}, \tag{A12}$$

and

$$n_S = n_B/2 = -I_0/(eu_SA). \tag{A13}$$

Setting V_S, n_S, and u_S by this procedure assures that E, V, u_i, and n_i will agree exactly with Bohm's theory of the dc sheath not only at the electrode, $x=x_{pe}$, but also over the entire range $x_S \leqslant x \leqslant x_{pe}$. For the rf sheath, we apply these same boundary conditions at the boundary point $x=x_n$, as shown in Eqs. (11)–(14), and obtain good agreement with experiment.

Admittedly, Bohm's analysis also allows solutions at $V_B < -kT_e/2e$, which would require $V_S < -2kT_e$, but boundary conditions based on such solutions do not give any better agreement with experiment. Also, there are solutions to Eqs. (A7) and (A8) with $E(x_S)>0$, and $V_S<-2kT_e$, but boundary conditions based on these solutions are in poorer agreement with experiment. Solutions with $V_S<-2kT_e$ also suf-

fer from another problem: if V_S is too negative, there will be conditions at high rf bias voltage where the sheath voltage becomes greater than V_S. Under such conditions, the step model has no solutions (or only nonphysical solutions with a negative sheath width) as shown by Gierling and Riemann (see Fig. 4 of Ref. [18]).

APPENDIX B: ANALYTIC APPROXIMATION

Analytic models for sheaths at very low bias frequencies are usually obtained by taking a dc sheath model and inserting a time-varying voltage in place of the dc sheath voltage. Such models assume that the ions cross the sheath instantaneously compared to the slowly varying sheath voltage. A better approximation, valid over a wider range of frequencies, can be obtained as follows. We acknowledge that the ions have a finite transit time, but assume that, over the time scale of ion transit, the sheath can be approximated by a step sheath moving at constant velocity. The solution for the moving sheath is then easily obtained by taking a dc sheath solution and shifting to a reference frame in which the sheath is moving with constant velocity u_s. Specifically, if the dc solutions for the sheath voltage and the other model parameters are denoted by $V'(x)$, $E'(x)$, $u_i'(x)$, and $n_i'(x)$ [with $n_e'(x)=0$], we obtain the time-varying solution by defining

$$V(x,t)=V'(x+u_s t), \tag{B1}$$

$$E(x,t)=E'(x+u_s t), \tag{B2}$$

$$n_i(x,t)=n_i'(x+u_s t), \tag{B3}$$

and

$$u_i(x,t)=u_i'(x+u_s t)-u_s. \tag{B4}$$

where u_s, the sheath velocity, is a constant. One can verify that these are valid solutions by substituting them into Eqs. (1)–(4). The time-dependent functions (V, E, n_i, and u_i) will satisfy those equations, provided that the time-independent functions (V', E', n_i', and u_i') satisfy the time-independent equations [Eqs. (1), (A1), (A2), and (4)].

Time derivatives in the laboratory reference frame, in which the sheath is moving, are related to space derivatives in the reference frame moving with the sheath:

$$\partial V/\partial t = u_s\, \partial V'/\partial x = -u_s E', \tag{B5}$$

$$\partial E/\partial t = u_s\, \partial E'/\partial x = e u_s n_i'/\varepsilon_0. \tag{B6}$$

The displacement current is obtained from Eqs. (7) and (B6):

$$I_d = -e\, n_i\, u_s A. \tag{B7}$$

Eliminating u_s using Eq. (B5) and n_i using $I_0=-e\, n_i\, u_i A$ we obtain

$$I_d = -I_0 E^{-1}(-m_i/2eV)^{1/2}\, dV/dt, \tag{B8}$$

where I_0 is the time-averaged ion current and E is the electric field, given in Eq. (A8). This result is almost the same as the Metze-Ernie-Oskam displacement current, which is obtained by instead substituting E from Eq. (A7).

The ion current is obtained by integrating the ion continuity equation, Eq. (3), starting at x_s, the position of the step:

$$I_i(x,t)=I_i(x_s,t)+e\, u_s A[n_i(x_s)-n_i(x)]. \tag{B9}$$

Here $I_i(x_s,t)$ is the ion current at the step, which is equal to the time-averaged ion current I_0. Simplifying, using Eqs. (A13) and (B5), we obtain

$$I_i(x,t)=-I_0+I_0 E^{-1}[(-m_i/2eV)^{1/2}-(m_i/4kT_e)^{1/2}]dV/dt. \tag{B10}$$

The analytic expression for the electric field from Eq. (A8) can be inserted into this equation, to give an analytic expression for the ion current in terms of the sheath voltage. The displacement current from Eq. (B8) and the electron current from Eq. (8) are then added to get an analytic equation for the total current of the rf sheath. The analytic equation is valid at least up to $\omega/\omega_i(x_B)=0.1$ (see Fig. 5). At higher ω/ω_i, the assumption that the sheath moves at constant velocity eventually becomes untenable, because the acceleration of the sheath, on the time scale of ion transit, becomes significant.

APPENDIX C: DEPENDENCE OF ION FLUX ON TRANSIT TIME

To derive an equation that relates the variations in transit time and ion flux, consider ions that start at a position x_s at time t_s, and arrive at a position x_f at time t_f. We define $\tau(t_f)$, the transit time, as a function of the arrival time, so that $t_s=t_f-\tau(t_f)$. Similarly, ions arriving at time $t_f'=t_f+\Delta t$ will have started at time $t_s'=t_f'-\tau(t_f')$. If ions are not created, are not destroyed, and do not suffer collisions in the region between x_s and x_f, then all ions arriving during the interval (of length Δt) between t_f and t_f' will have started during the interval [of length $\Delta t+\tau(t_f)-\tau(t_f')$] between t_s and t_s'. If $\tau(t_f)\neq\tau(t_f')$, the two intervals are of different lengths, and the ion fluxes at the start and the end, $\Phi(x_s,t_s)$ and $\Phi(x_f,t_f)$, must be different. Specifically,

$$\Phi(x_f,t_f)\Delta t=\Phi(x_s,t_s)[\Delta t+\tau(t_f)-\tau(t_f')]. \tag{C1}$$

Or, in terms of the derivative of the transit time $d\tau(t_f)/dt_f$,

$$\Phi(x_f,t_f)=\Phi(x_s,t_s)[1-d\tau(t_f)/dt_f]. \tag{C2}$$

We choose $x_f=x_{\mathrm{pe}}$, the position of the electrode, and choose x_s to be a position within the plasma, far from the electrode, where the electric field and the ion flux are not significantly perturbed by the application of rf bias and thus can be considered constant in time. Thus, the ion current at the electrode

$$I_i(x_{\mathrm{pe}},t_f)=I_0[1-d\tau(t_f)/dt_f] \tag{C3}$$

is the sum of a time-independent part (which is the time-averaged ion current I_0) and a time-dependent part, which arises from the variation in ion transit times.

[1] B. E. Thompson, K. D. Allen, A. D. Richards, and H. H. Sawin, J. Appl. Phys. **59**, 1890 (1986).
[2] K. D. Allen and H. H. Sawin, J. Electrochem. Soc. **133**, 2326 (1986).
[3] A. J. Van Roosmalen, Appl. Phys. Lett. **42**, 416 (1983).
[4] B. Andries, G. Ravel, and L. Peccoud, J. Vac. Sci. Technol. A **7**, 2774 (1989).
[5] Y. Ra and C.-H. Chen, J. Vac. Sci. Technol. A **11**, 2911 (1993).
[6] M. A. Sobolewski, Appl. Phys. Lett. **72**, 1146 (1998).
[7] S. Rauf and M. J. Kushner, Appl. Phys. Lett. **73**, 2730 (1998).
[8] M. Klick, W. Rehak, and M. Kammeyer, Jpn. J. Appl. Phys., Part 1 **36**, 4625 (1997).
[9] M. A. Lieberman, IEEE Trans. Plasma Sci. **16**, 638 (1988).
[10] M. A. Lieberman, IEEE Trans. Plasma Sci. **17**, 338 (1989).
[11] P. M. Vallinga, P. M. Meijer, and F. J. de Hoog, J. Phys. D **22**, 1650 (1989).
[12] V. A. Godyak and N. Stemberg, Phys. Rev. A **42**, 2299 (1990).
[13] K. Bornig, Appl. Phys. Lett. **60**, 1553 (1992).
[14] N. Sternberg and V. A. Godyak, J. Comput. Phys. **111**, 347 (1994).
[15] M. A. Sobolewski, Phys. Rev. E **56**, 1001 (1997).
[16] S. Biehler, Appl. Phys. Lett. **54**, 317 (1989).
[17] M. Klick, J. Appl. Phys. **79**, 3445 (1996).
[18] J. Gierling and K. U. Riemann, J. Appl. Phys. **83**, 3521 (1998).
[19] F. R. Myers and T. S. Cale, J. Electrochem. Soc. **139**, 3587 (1992).
[20] A. M. Pointu, Appl. Phys. Lett. **48**, 762 (1986).
[21] A. M. Pointu, J. Appl. Phys. **60**, 4113 (1986).
[22] M. Klick, Phys. Rev. E **47**, 591 (1993).
[23] A. Metze, D. W. Ernie, and H. J. Oskam, J. Appl. Phys. **60**, 3081 (1986).
[24] P. M. Vallinga and F. J. de Hoog, J. Phys. D **22**, 925 (1989).
[25] P. A. Miller and M. E. Riley, J. Appl. Phys. **82**, 3689 (1997).
[26] T. Panagopoulos and D. J. Economou, J. Appl. Phys. **85**, 3435 (1999).
[27] E. A. Edelberg and E. S. Aydil, J. Appl. Phys. **86**, 4799 (1999).
[28] W. J. Goedheer and P. M. Meijer, IEEE Trans. Plasma Sci. **19**, 245 (1991).
[29] D. Martin and H. Oechsner, Vacuum **47**, 1017 (1996).
[30] D. Bose, T. R. Govindan, and M. Meyyappan, J. Appl. Phys. **87**, 7176 (2000).
[31] M. A. Sobolewski, Appl. Phys. Lett. **70**, 1049 (1997).
[32] M. A. Sobolewski, Phys. Rev. E **59**, 1059 (1999).
[33] P. A. Miller, G. A. Hebner, K. E. Greenberg, P. D. Pochan, and B. P. Aragon, J. Res. Natl. Inst. Stand. Technol. **100**, 427 (1995).
[34] J. R. Woodworth, M. E. Riley, D. C. Meister, B. P. Aragon, M. S. Le, and H. H. Sawin, J. Appl. Phys. **80**, 1304 (1996).
[35] A. Schwabedissen, E. C. Benck, and J. R. Roberts, Phys. Rev. E **55**, 3450 (1997).
[36] A. Schwabedissen (unpublished).
[37] E. C. Benck, A. Schwabedissen, A. Gates, and J. R. Roberts, J. Vac. Sci. Technol. A **16**, 306 (1998).
[38] M. A. Sobolewski, Y. Wang, and J. K. Olthoff, J. Appl. Phys. **85**, 3966 (1999).
[39] Y. Wang and J. K. Olthoff, J. Appl. Phys. **85**, 6358 (1999).
[40] A. V. Phelps, J. Appl. Phys. **76**, 747 (1994).
[41] D. Bohm, in *The Characteristics of Electrical Discharges in Magnetic Fields*, edited by A. Guthrie and R. K. Wakerling (McGraw-Hill, New York, 1949), p. 77.
[42] M. A. Sobolewski, J. Vac. Sci. Technol. A **10**, 3550 (1992).
[43] M. A. Sobolewski, IEEE Trans. Plasma Sci. **23**, 1006 (1995).
[44] R. L. F. Boyd and J. B. Thompson, Proc. R. Soc. London, Ser. A **252**, 102 (1959).
[45] U. Czarnetzki, D. Luggenhölscher, and H. F. Döbele, Plasma Sources Sci. Technol. **8**, 230 (1999).